Structure of the silicon vacancy in 6*H*-SiC after annealing identified as the carbon vacancy–carbon antisite pair

Th. Lingner, S. Greulich-Weber, and J.-M. Spaeth
Experimental Physics, Physics Department, University of Paderborn, D-33098 Paderborn, Germany

U. Gerstmann, E. Rauls, Z. Hajnal, Th. Frauenheim, and H. Overhof
Theoretical Physics, Physics Department, University of Paderborn, D-33098 Paderborn, Germany
(Received 29 June 2001; published 7 December 2001)

We investigated radiation-induced defects in neutron-irradiated and subsequently annealed 6*H*-silicon carbide (SiC) with electron paramagnetic resonance (EPR), the magnetic circular dichroism of the absorption (MCDA), and MCDA-detected EPR (MCDA-EPR). In samples annealed beyond the annealing temperature of the isolated silicon vacancy we observed photoinduced EPR spectra of spin $S=1$ centers that occur in orientations expected for nearest neighbor pair defects. EPR spectra of the defect on the three inequivalent lattice sites were resolved and attributed to optical transitions between photon energies of 999 and 1075 meV by MCDA-EPR. The resolved hyperfine structure indicates the presence of one single carbon nucleus and several silicon ligand nuclei. These experimental findings are interpreted with help of total energy and spin density data obtained from the standard local-spin density approximation of the density-functional theory, using relaxed defect geometries obtained from the self-consistent charge density-functional theory based tight binding scheme. We have checked several defect models of which only the photoexcited spin triplet state of the carbon antisite–carbon vacancy pair (C_{Si}-V_C) in the doubly positive charge state can explain all experimental findings. We propose that the (C_{Si}-V_C) defect is formed from the isolated silicon vacancy as an annealing product by the movement of a carbon neighbor into the vacancy.

DOI: 10.1103/PhysRevB.64.245212 PACS number(s): 71.55.Ht, 76.30.Da, 71.15.Mb, 71.15.Qe

I. INTRODUCTION

Its unique electronic and thermal properties make silicon carbide (SiC) suitable for many high power, high frequency, and high temperature electronic applications.[1] As most dopants diffuse prohibitively slowly into SiC, ion implantation is the preferred doping method in device fabrication. However, the implantation process inevitably creates radiation-induced defects. Although sometimes helpful as recombination centers reducing the carrier lifetime in high frequency devices or to create semi-insulating areas,[2] radiation-induced defects usually are unwanted by-products of the implantation process compensating the implanted dopants. In order to gain control over the radiation damage it is helpful to investigate the annealing behavior of these defects and to identify the follow-up defects created by the annealing of the primary radiation defects. Of particular interest is of course the electrical and optical activity of the follow-up defects.

A basic radiation defect in SiC is the isolated silicon vacancy (V_{Si}) which has been thoroughly investigated both experimentally[3–7] and theoretically.[7–12] V_{Si} anneals out at 750 °C (Refs. 3,4) with an activation energy of 2.2 ± 0.3 eV.[4] In elemental semiconductors a lattice vacancy can anneal out by moving through the lattice. In compound semiconductors the situation is more complicated, because chains of antisite defects must be created if the vacancy moves by nearest neighbor hops. It has recently been proposed that the first step in such an annealing process, the formation of the C_{Si}-V_C antisite-vacancy pair from the isolated silicon vacancy, is a quite probable process.[9] But there was no experimental evidence for the presence of the pair after annealing.

In this paper we show that the *P*6/*P*7 spectrum observed by light-induced electron paramagnetic resonance (EPR) (Ref. 13) and by optically detected magnetic resonance (ODMR) (Refs. 14,15) is most likely due to a photoexcited spin-triplet state of the C_{Si}-V_C pair. Whereas the ground state of the defect in 6*H*-SiC is diamagnetic and not accessible to magnetic resonance, the photoexcited paramagnetic triplet state was observed for all inequivalent lattice sites and in all orientations with EPR, the magnetic circular dichroism of the absorption (MCDA) and MCDA-detected EPR (MCDA-EPR).

To confirm the identification of the C_{Si}-V_C pair, we have performed theoretical investigations of several pair defect models. We find C_{Si}-V_C in the charge state $+2$ to be the only intrinsic nearest neighbor pair defect that is diamagnetic in its ground state and has a photoexcited spin-triplet state that can give rise to the hyperfine structure and the optical transitions observed experimentally. We can, of course, not prove unambiguously that the silicon vacancy is the origin of the proposed annealing process. We note however that the pair is observed after irradiation and subsequent annealing above the annealing temperature of the silicon vacancy. Therefore, V_{Si} seems to be the ideal candidate for the precursor of the C_{Si}-V_C pair.

Our paper is organized as follows. In Sec. II, the samples and the experimental techniques are described. Section III introduces the computational methods. In Sec. IV, the experimental results are presented, whereas in Sec. V, the results of theoretical calculations are presented and related to the experimental findings. We close with a brief discussion of the microscopic structure and the electronic properties of the C_{Si}-V_C pair defect.

II. EXPERIMENTAL

The samples were nitrogen-doped (10^{18} cm^{-3}) 6*H*-SiC grown by the sublimation sandwich method.[16] They were irradiated with reactor neutrons at a dose of 2×10^{18} cm^{-2} and then annealed for two minutes at 600, 1000, and 1200 °C, respectively. One sample of the batch was left unirradiated, and another sample was irradiated but not annealed. Since the unirradiated samples were nitrogen doped, they must be regarded as *n*-type material. However, due to irradiation the position of the Fermi level is lowered by an unknown amount. In addition, because of possible inhomogeneties the positions of the band edges relative to the Fermi level may vary over the whole sample.

EPR was measured in a custom made *X*-band (9.8 GHz) spectrometer with a cylindrical TE_{011} cavity. The sample temperature was $T=7$ K. During the measurements the samples were illuminated with the white light of a halogen lamp.

The MCDA is the differential absorption of right- and left-circularly polarized light propagating parallel to an external magnetic field. The MCDA of a point defect arises from spin-conserving optical transitions from a paramagnetic ground state to higher states. At sufficiently low temperatures, the Zeeman sublevels of the ground state differ in their occupation numbers, leading to a temperature- and field-dependent spin polarization. The paramagnetic part of the MCDA is proportional to this spin polarization, see, e.g., Ref. 27. To detect an EPR signal via the MCDA, EPR transitions are induced between the Zeeman sublevels. Under partial saturation conditions—i.e., when the EPR transition rate is comparable to the spin-lattice relaxation time—the EPR transitions alter the occupation numbers, thus changing the spin polarization. Thereby, the EPR transitions are observed as a change of the MCDA signal intensity.[27]

To measure the MCDA and MCDA-EPR, the light of a halogen bulb was passed through a 500 mm single grating monochromator (Spex 500M) and a combination of linear polarizer and acousto-optical modulator operating at 25 kHz. The light transmitted by the sample was detected with a germanium infrared detector (North Coast EO-817J). The detector signal was demodulated in a lock-in amplifier using the modulator frequency as reference. The samples were immersed in superfluid helium ($T=1.5$ K) in a bath cryostat equipped with a superconducting magnet. For the MCDA-EPR measurements *K* band (24 GHz) microwaves from a 500 mW reflex klystron were coupled into a cylindrical cavity with optical access in the magnetic field direction. Some MCDA-EPR experiments required additional optical excitation of the sample with the visible (457.9–515.5 nm, 200 mW/mm^2) or the UV (351–363.8 nm, 30 mW/mm^2) multiline light of an argon ion laser. We will abbreviate this with laser excitation.

III. COMPUTATIONAL

We have used the self-consistent linear muffin-tin orbitals method in the atomic spheres approximation (LMTO-ASA),[17] treating exchange and correlation effects within the framework of the local spin density approximation of the density-functional theory (LSDA-DFT). In a Green's function approach, the problem separates into two parts. First, the Green's function $g^0(E)$ of the perfect crystal is constructed from the bandstructure of the infinite perfect crystal. Then the Green's function $g(E)$ of the impurity is obtained by solving the Dyson equation

$$\{1+g^0(E)[\Delta P(E)-\Delta S]\}g(E)=g^0(E) \tag{1}$$

written in terms of the Green's function g^0 of the perfect crystal. Here $\Delta P=P-P^0$ is the perturbation of the so-called potential function describing the electronic structure, and the nondiagonal matrix $\Delta S=S-S^0$ is the relaxation-induced change of the LMTO-ASA structure constants.

The use of a Green's function method allows one to investigate an isolated defect embedded in an otherwise perfect infinite crystal. For strongly localized defects ΔP is large only in a small region around the defect. In fact, for the defects investigated in this work, it turns out to be sufficient to solve the Dyson equation Eq. (1) within a perturbed region containing 28 atoms around the defect. Outside this region, g is approximated by g^0. Usually, the LSDA underestimates the fundamental band gap. When constructing the Green's function $g^0(E)$ of the unperturbed crystal, this problem is circumvented by the scissors operator technique[20,21] adjusting the energy of the fundamental gap to the experimental value of 3.1 eV for 6*H*-SiC.

In this work, we used the LMTO-ASA method to calculate total energies and the magnetization density distribution of vacancy-related defects in excited states. As already outlined in Ref. 22, the DFT describes not only the ground state of a many-body system, but can also be used to calculate total energies for those excited states that transform according to a different irreducible representation than all lower-lying many-body states. This treatment has recently been applied to transition metal related defects in group-III nitrides[23] and to the $^5A_2$ excited state of the neutral vacancy in diamond.[24] In these cases, total energies, transition energies, and hyperfine interactions[26] of the excited states are obtained with a similar precision as for ground states.

In the past, a vanishing ΔS had to be assumed, in order to minimize the size of the matrices and thus to optimize the performance of the numerical calculations. This approximation, though, neglects the lattice relaxations. To cope with this main shortcoming of the method in its former version, we have used a combined approach: The atomic positions of the relaxed structure were obtained from additional calculations within the self-consistent charge density-functional theory based tight-binding (SCC-DFTB) scheme.[25] In a $(5\times6\times1)$ supercell model of the 6*H* polytype containing 300 atoms the defect and its nearest and next nearest neighbors have been relaxed. The relaxation energies have been added to the LMTO total energies, resulting in $E=E_{\mathrm{LMTO}}+\Delta E^{\mathrm{relax}}_{\mathrm{DFTB}}$. Assuming that the lattice relaxation is almost independent of the spin polarization, this should be a good estimate for a fully self-consistent treatment in which the effects of spin polarization and lattice relaxation would be considered simultaneously.

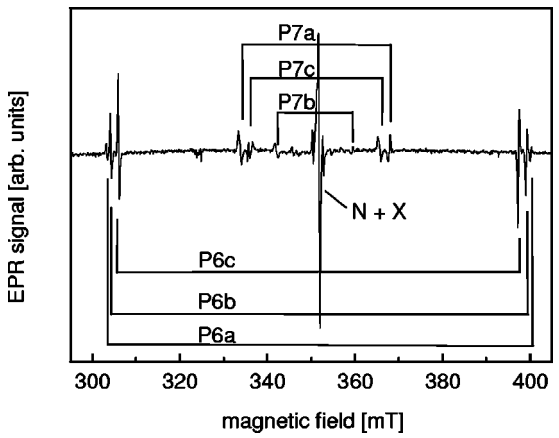

FIG. 1. *X*-band EPR spectrum of neutron-irradiated and at 1000 °C annealed 6*H*-SiC measured with the magnetic field parallel to the *c*-axis of the crystal. Under illumination of the sample, six spin-triplet spectra labeled $P6a,b,c$, and $P7a,b,c$ are measured. The central lines labeled $N+X$ arise from the nitrogen donor and a superimposed line of unknown origin.

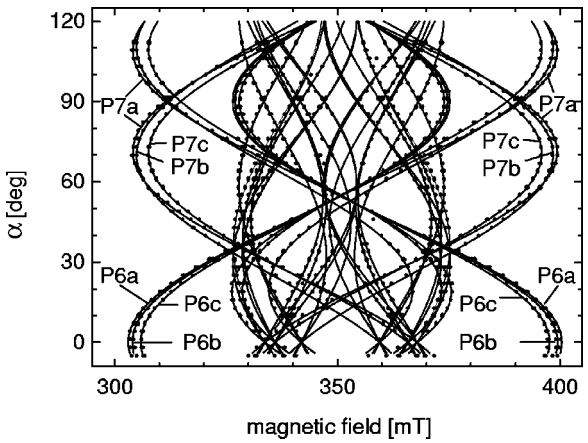

FIG. 2. *X*-band EPR angular dependence of the $P6a,b,c$ and $P7a,b,c$ spectra in 6*H*-SiC. α denotes the angle between the *c*-axis and the magnetic field, which was rotated in a plane that was misoriented by 5° to a (1120) plane. Dots indicate the experimental data. The solid lines show the result of a calculation using the parameters given in Table I. The microwave frequency was 9.871 GHz.

In addition to the total energy, lattice relaxation around a defect also modifies the magnetization density distribution and thus influences the hyperfine interactions. Starting from the relaxed structures obtained with SCC-DFTB, the hyperfine interactions have been calculated within an extended version of the LMTO-ASA Green's function method. Relaxation-induced changes in the structure constants ΔS for each atom are considered for its nearest and next nearest neighbors. The solution of Eq. (1) then leads to more accurate particle and magnetization densities, especially in the regions near the displaced nuclei.

IV. EXPERIMENTAL RESULTS AND ANALYSIS

A. EPR spectrum

The EPR signal of neutron-irradiated and annealed 6*H*-SiC (Fig. 1) consists of six spin triplet ($S=1$) spectra. Their angular dependence (Fig. 2) was analyzed using the spin Hamiltonian

$$H=\mu_B g\mathbf{B}\cdot\mathbf{S}+D\left(S_z^2+\frac{1}{3}S(S+1)\right)+E(S_x^2-S_y^2) \qquad (2)$$

with an electron spin $S=1$ and parameters given in Table I. Here, μ_B is the Bohr magneton, D is the axially symmetric part of the fine structure interaction, E is the anisotropy parameter, and Θ is the angle between the principal axis z of the fine structure tensor and the c axis of the crystal. No anisotropy of the g value was observed within $g=2.003\pm0.001$. For three of the centers, labeled $P6a$, b, and c, the principal axis z of the fine structure tensor is parallel to the *c*-axis of the crystal (axial orientations). The other three centers, labeled $P7a$, b, and c exist in six orientations each. Their z axes are oriented in one of the six $\{1120\}$ planes at an angle Θ to the c axis (basal orientations), see also Table I. The notations $P6$ and $P7$ for the axial and the basal orientations, respectively, are adopted from Vainer and Il'in,[13] and the letters a, b, and c denote the three different spectra of each orientation. As already mentioned by these authors, the vanishing anisotropic part of the fine structure tensor E indicates C_{3v}-symmetry for the $P6$ centers, whereas for the $P7$ centers (with nonvanishing E) C_{1h}-symmetry must be assumed.

The six $P6/P7$ spectra could be measured in the samples annealed at 600, 1000, and 1200 °C, but they were neither found in the unannealed sample nor in the unirradiated sample of the same batch. Their highest intensity has been measured in the sample annealed at 1000 °C. The spectra emerged only during illumination of the sample with photon energies above 1.1 ± 0.1 eV and hence belong to a photoexcited state. In addition to the $P6/P7$ spectra, the well-known EPR signal of the nitrogen donor superimposed on another line of unknown origin (X) was measured (Fig. 1). Only this unknown line X remains detectable in the dark.

The high field lines of the $P6/P7$ spectra are inverted due to induced microwave emission from the EPR transition. This proves that the occupation of the magnetic sublevels of

TABLE I. g values, fine structure parameters D and E and the angle Θ between the principal axis z of the fine structure tensor and the c axis of the crystal, determined from the angular dependence of the EPR signal using the spin-Hamiltonian Eq. (2). The sample temperature was 7 K. The photon energy of the corresponding optical intracenter transition was determined by MCDA-EPR.

Center	g	D [10^{-4} cm^{-1}]	E	Θ [°]	$h\nu$ [meV]
$P6a$	2.003	456	0	0.0	1075
$P6b$	2.003	447	0	0.0	1048
$P6c$	2.003	430	0	0.0	1011
$P7a$	2.003	449	−4	71.2	1049
$P7b$	2.003	441	46	70.0	1030
$P7c$	2.003	416	−1	70.5	999

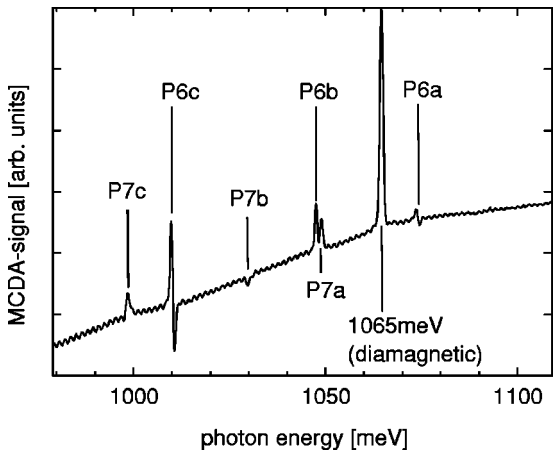

FIG. 3. MCDA spectrum of the $P6/P7$ centers, recorded with the c axis at an angle $\alpha = 20°$ to the magnetic field ($B = 2$ T) with laser excitation. In the labelled lines, the corresponding MCDA-EPR spectra (Table I, Fig. 4) were measured. The periodic background signal is caused by interferences between the polished faces of the thin birefringent crystal.

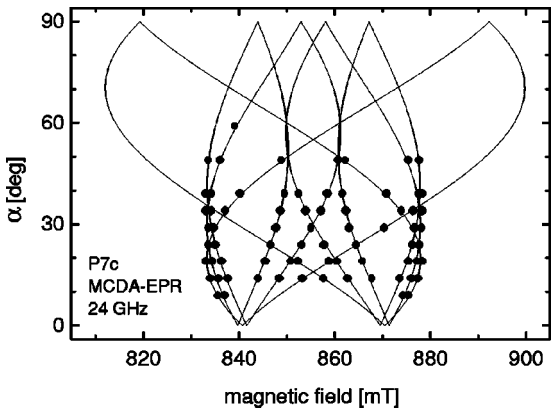

FIG. 4. Angular dependence of the $P7c$ MCDA-EPR signal, detected via the 999 meV MCDA line. α denotes the angle between the c axis and the magnetic field, which was rotated in a plane that was misoriented by 5° to a (1120) plane. The range of α for which experimental data could be acquired is restricted by weak MCDA signals for small α and by constraints due to the optical setup for large α. The solid lines are calculated using the parameters of the $P7c$ center given in Table I. The microwave frequency is 24.03 GHz.

the defect strongly deviates from that in thermal equilibrium.[27] The intensity of the EPR spectra varies with the angle α between the magnetic field and the c axis of the crystal. It reaches its maximum for the magnetic field approximately parallel to the principal axis of the fine structure tensor.

B. MCDA, MCDA-EPR and fine structure

The MCDA and PL spectra of the unannealed samples and those annealed at 600 °C show the optical transitions of the silicon vacancy related defect reported in Ref. 5. The signal of this defect is absent after annealing at 1000 °C. The MCDA spectrum (Fig. 3) shows six lines with temperature and field dependent intensities that originate from a paramagnetic ground state. An additional MCDA line with diamagnetic behavior was found at 1065 meV (Fig. 3). The intensity of the $P6$ MCDA lines was highest with the magnetic field parallel to the c axis of the crystal ($\alpha = 0°$). The $P7$ lines, in contrast, were best observed around $\alpha = 25°$. The intensity of the $P6/P7$ lines increased upon laser excitation or upon prolonged exposure of the sample to the MCDA measurement light (with photon energies of 1.0–1.1 eV). The diamagnetic line at 1065 meV was only observed upon laser excitation.

The MCDA-EPR method allows one to detect each EPR spectrum separately and to attribute it to the corresponding optical transition. In each paramagnetic MCDA line (Fig. 3) a single EPR spectrum from Table I was detectable with MCDA-EPR. For example, the MCDA-EPR spectrum detected in the 999 meV MCDA line (Fig. 4) can be described with the EPR parameters of the $P7c$ center. This unambiguously proves that the six EPR spectra belong to different atomic configurations with different electronic levels. In addition, it is noted that the higher the value of the fine structure constant D, the larger is the photon energy of the optical transition.

The magneto-optical properties of the $P6/P7$ centers depend on the illumination of the sample. As long as only the weak light necessary to measure the MCDA is present, both the high field and the low field MCDA-EPR transitions reduce the MCDA line intensity, i.e., both transitions decrease the spin polarization. The high field line is the more intense one, indicating a positive sign of the fine structure constant D. The spin-lattice relaxation time T_1 is of the order of minutes. Upon laser excitation with the UV (351–363.8 nm) or the visible (457.9–515.5 nm) light of an argon ion laser, the high field MCDA-EPR line inverts, i.e., the high field EPR transition now increases the spin polarization. Simultaneously a shorter relaxation time of the order of seconds is observed. The inversion of the high field line indicates that the occupation number of the $m_s = 0$ level exceeds that of the $m_s = \pm 1$ levels (Fig. 5).

C. Hyperfine structure

The hyperfine structure of an EPR signal arises from the magnetic interaction of the unpaired electrons with the nuclear magnetic moments of the nuclei around the defect. The $P6$ and $P7$ spectra have symmetric hyperfine splittings due to the interaction with $I = 1/2$ nuclei. Two sets of hyperfine lines were observed (Fig. 6). The inner set consists of two hyperfine lines split by 12 ± 2 MHz for **B** parallel to the z axis, and each line has an intensity ratio of $15 \pm 5\%$ to the central line. The hyperfine lines partly overlap with the central line, and they appear to be broadened. This set was observed for all $P6$ and $P7$ spectra at orientations near **B** parallel to the z axis. For other orientations, the signal intensities were too weak to resolve the hyperfine lines.

The outer set consists of two weak hyperfine lines split by 48 ± 2 MHz with an intensity ratio of $0.7 \pm 0.2\%$ to the central line. Due to weak signal intensities and the overlap with the other EPR spectra, this set could only be analyzed for the

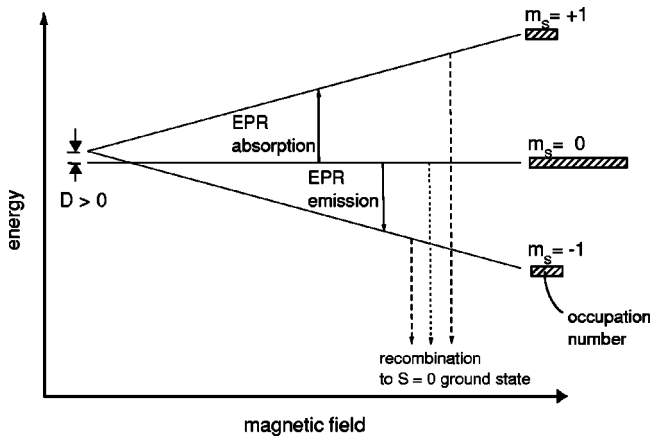

FIG. 5. The recombination from the photoexcited spin triplet state to the singlet ground state is weakly allowed for the $m_s = \pm 1$ Zeeman levels, but forbidden for the $m_s = 0$ level. If the spin-lattice-relaxation time is long compared to the lifetime of the triplet state, this leads to a higher population of the $m_s = 0$ level compared to the $m_s = \pm 1$ levels. Consequently, in case of a positive fine structure constant *D*, the high field lines invert.

*P*6*c* spectrum and only at orientations near **B** parallel to the *z* axis. So the observed splitting corresponds to $A_{||} = a + 2b$. Thus, it was not possible to determine the isotropic part *a* and the anisotropic part *b* separately.

D. Discussion

In SiC, several spin triplet systems have already been attributed to pair defects: The *P*6/*P*7 spectra[13] in 6*H*-SiC were attributed to nearest-neighbor vacancy pairs.[13,14] The so-called abcd ODMR spectra in 6*H*-SiC (Ref. 14) and the *L*3 center in 3C-SiC (Ref. 15) have been suggested to be complexes involving a silicon vacancy, possibly the silicon

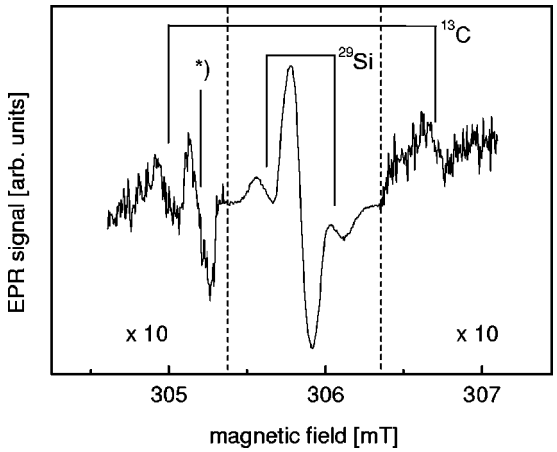

FIG. 6. Hyperfine structure of the *P*6*c* low field EPR line for **B** parallel to the *c* axis. The intensity ratio of the hyperfine satellites to the central line corresponds to the interaction with four to eight silicon nuclei for the inner pair and one carbon nucleus for the outer pair. The outer parts of the spectrum are scaled by a factor of 10 with respect to the inner part. The line marked with an asterisk is due to a different unknown center.

vacancy–silicon antisite pair. During the last years, these centers have been reported as common defects in many SiC polytypes. They were observed in as-grown bulk 6*H*-SiC[14], in rapidly grown epitaxial layers,[14] in electron-irradiated material,[14] after thermal quenching and subsequent annealing between 800 and 1200 °C,[13] and in electron-irradiated 3C-SiC after annealing above 750 °C.[15] A similar spin triplet spectrum (*G*6 spectrum) was also found in 4*H*-, 6*H*- and 15*R*-SiC irradiated with neutrons or alpha particles and subsequently annealed between 400 °C and 900 °C.[28]

All *P*6 and *P*7 spectra discussed in this work have similar *g* values, similar values of the fine structure constant *D*, and similar photon energies of the optical transitions. There are three centers of the *P*6 type (C_{3v}-symmetry) and three centers of the *P*7 type (C_{1h}-symmetry). We assume that the three inequivalent lattice sites in 6*H*-SiC give rise to the splitting into three different spectra of each type.

The fine structure constants *D* measured by us deviate from those of similar spectra published elsewhere[13,28,14] by a few percent. It is known though, that the value of *D* of the *G*6 spectrum is strongly temperature dependent, increasing from 340×10^{-4} cm^{-1} at $T = 300$ K to 397×10^{-4} cm^{-1} at $T = 100$ K.[28] As the published data were obtained at different sample temperatures, the differences in the EPR parameters are thought to arise from this temperature dependence. We suppose, that the *G*6 spectrum in Ref. 28, the *P*6 spectrum in Ref. 13, the *a* and *b* spectra in Ref. 14, and the *P*6 spectra in our results are due to the same type of centers in the axial orientations, and that the *P*7 spectrum in Ref. 28, the *c* and *d* spectra in Ref. 14 and the *P*7 spectra in our results are also due to the same defect in the basal orientations.

The angle Θ between the principal *z* axis of the fine structure tensor and the *c* axis of the crystal is zero for the *P*6 centers, and with an average value of 70.56° (see Table I) it is close to the ideal tetrahedral angle (70.529°) for the *P*7 centers. As already pointed out by Vainer and Il'in[13] and by Son *et al.*,[14] these orientations can be explained with a nearest-neighbor pair defect: in case of the *P*6 centers the neighboring sites are oriented in the axial bond directions parallel to the *c* axis, and in case of the *P*7 centers they are oriented in the basal bond directions at angles near 70.5° to the *c* axis. The small deviations of the angle Θ from the ideal tetrahedral angle can be attributed to lattice relaxation around the defect.

As the *P*6/*P*7 spectra were not measured in our samples except after neutron irradiation and subsequent annealing, we assume in agreement, with Refs. 13,14,28 that the defect is not related to extrinsic impurities. Its character of a nearest neighbor pair defect and its intrinsic nature limit the set of possible models to the vacancy pair V_{Si}-V_C, the antisite pair C_{Si}-Si_C, and the vacancy-antisite pairs $V_{Si}-Si_C$ and C_{Si}-V_C.

The key to distinguish between these models is the hyperfine interaction with silicon and carbon atoms. The natural abundance of isotopes with a nuclear magnetic moment is 4.7% for silicon (^{29}Si, $I = 1/2$) and 1.1% for carbon (^{13}C, $I = 1/2$). Thus, the statistical prediction for the intensity of one hyperfine line with respect to the central line is 0.6% for one carbon nucleus and 2.4% for one silicon nucleus. The outer hyperfine lines of the *P*6*c* spectrum ($A_{||} = 48$ MHz), each

with an intensity ratio to the central line of $0.7\pm0.2\%$, are therefore most likely due to the interaction with a single carbon nucleus. The intensity ratio ($15\pm5\%$) of the inner hyperfine lines ($A_{||}=12$ MHz) can be explained with the interaction with four to eight silicon neighbors. The broadening of these hyperfine lines may be an indication of superimposed contributions from different silicon neighbor shells with similar hyperfine constants, in other words, the four to eight silicon neighbors need not all be equivalent.

Our experimental results can be summarized as follows: we have measured the photoexcited spin-triplet state of a defect with the symmetry properties of a nearest-neighbor pair. The defect was observed in each orientation and for each of the inequivalent lattice sites. The spin-triplet state can be generated upon photoexcitation with photon energies above 1.1 eV, and is itself the ground state of an optical transition with photon energies of about 1 eV. The defect is most probably of intrinsic nature and occurs after irradiation and subsequent annealing at temperatures above the annealing temperature of the silicon vacancy. The hyperfine structure indicates the presence of one prominent carbon nucleus.

V. COMPUTATIONAL RESULTS AND DISCUSSION

In the following, we discuss the possible models described in the section above theoretically. Since we find only small differences in defect geometries and formation energies between hexagonal and cubic sites, we will limit our discussion here to the cubic sites.

A. Si_C-V_{Si}

In agreement with former theoretical results[29], this pair defect was calculated in all charge states to be unstable against recombination to V_C. Furthermore, in this defect structure there is no single prominent carbon nucleus. Therefore, it must be eliminated from the list of possible candidates.

B. V_{Si}-V_C

The divacancy V_{Si}-V_C was originally proposed in Ref. 13 to explain the $P6/P7$ signal. Indeed, this defect model can explain most of the experimental findings concerning the excitation scheme and the hyperfine splittings very well. Especially, we calculated the hyperfine parameters for the neutral pair in an excited state ($A_{\|}=65$ MHz for the three equivalent ^{13}C ligands and $A_{\|}=-13$ MHz for the three equivalent ^{29}Si ligands) to be in good agreement with the experimentally observed values. However, with its three equivalent carbon ligands it clearly deviates from the experimental finding of one single prominent ^{13}C nucleus of a defect pair in C_{3v}-symmetry.

C. C_{Si}-Si_C

In Ref. 30 the authors claim the antisite pair to exist in the charge states $+4$ to -1. The existence of the charge states $+4$ to 0 was confirmed by our total energy calculations, but the negative charge state could only be achieved by occupying the conduction band. For all these charge states we obtain only a small symmetry-induced splitting (<0.2 eV) between the a_1 and e single-particle defect levels. Therefore, the estimates for the excitation energies (also <0.2 eV) strongly deviate from the experimentally observed values of above 1 eV (Table I). Hence, the antisite pair cannot explain the optical transitions of the $P6/P7$ center.

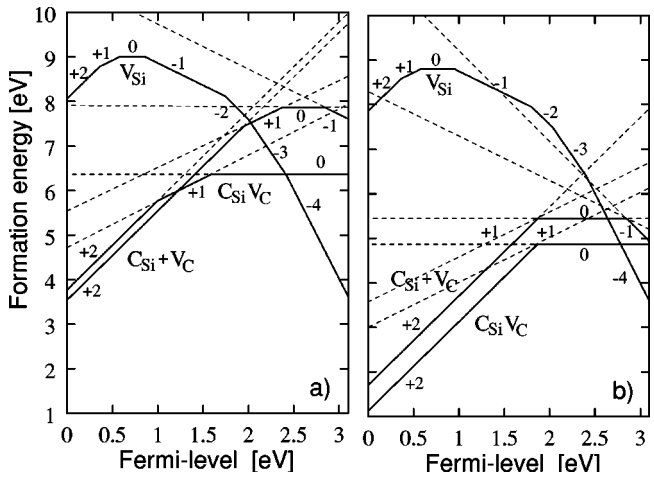

FIG. 7. Formation energies of the (a) unrelaxed and (b) relaxed silicon vacancy (V_{Si}), carbon-antisite carbon-vacancy pair (C_{Si}-V_C), and sum of formation energies of the isolated carbon antisite and the isolated carbon vacancy ($C_{Si}+V_C$).

D. C_{Si}-V_C

The final candidate is the carbon antisite–carbon vacancy pair. Similar defects are known from other binary semiconductors. The gallium vacancy in GaAs can, e.g., transform to an As_{Ga}-V_{As} antisite-vacancy pair.[31–33] There are similar speculations about an EPR signal arising from an excited $S=1$ state of a P_{Ga}-V_P pair in GaP (see Ref. 34, and references therein).

The stability of a defect can be judged from its formation energy which depends on the Fermi level. Figure 7(a) shows the total energies E_{LMTO} calculated with the LMTO-ASA Green's function approach, including the spin polarization of the electrons but neglecting lattice relaxation. In Fig. 7(b) relaxation induced effects are taken into account, as described in Sec. III.

The line denoted with "$C_{Si}+V_C$" gives the sum of the formation energies for the isolated antisite and the vacancy, while the curve "$C_{Si}V_C$" belongs to the antisite-vacancy pair. The curve "$C_{Si}+V_C$" can be directly compared to results for the isolated carbon vacancy, since—in contrast to the isolated Si_C antisite—the isolated C_{Si} antisite exists in the neutral charge state only[10] and therefore just yields a constant energy shift. Thus, from part (b) of Fig. 7 it can be seen, that our combined approach reproduces the results obtained with other *ab initio* methods, including, e.g., a tendency towards negative-U effects which is discussed controversially in the literature. The experimental observation of an EPR signal from V_C^+ (Refs. 4,35) strongly contradicts the theoretical findings of a $++/0$ negative-U transition.[12] The reason for

this debate becomes clear from our calculations, showing that the difference between the charge transfer levels (<0.05 eV) is below the numerical accuracy of state-of-the-art calculations. The same is true for the antisite-vacancy pair C_{Si}-V_C, where it cannot be decided whether a $(++/0)$ negative-U transition occurs or not.

At all positions of the Fermi level, the formation energy of the C_{Si}-V_C pair is ≈ 0.6 eV lower than the sum of formation energies of the isolated carbon antisite and the isolated carbon vacancy. In addition, the migration barrier for the dissociation was calculated to exceed 4.5 eV. Therefore, C_{Si}-V_C is expected to be stable against dissociation into its components.

In irradiated material, the *P*6/*P*7 spectra typically appear after annealing above 750 °C, which is the annealing temperature of the silicon vacancy.[3,4] Former SCC-DFTB-calculations indicate a metastability of the silicon vacancy:[9] with an energy gain of 1.6 eV a carbon neighbor can migrate into the silicon vacancy, resulting in the C_{Si}-V_C pair. The calculated energy barrier for this process is 1.7 eV for the neutral charge state.[9] This value is close to the activation energy found experimentally for the annealing of the negatively charged silicon vacancy in 3C-SiC (2.2 ± 0.3 eV).[4]

At first sight the silicon vacancy in 6*H*-SiC seems to be a simple defect. Nevertheless, configuration interaction (CI) (Ref. 19) calculations[18,6] have shown that for the neutral charge state the high spin prediction of LSDA calculations must be corrected to a diamagnetic low spin configuration. However, the corresponding energy lowering is only ≈ 0.17 eV,[18] that means much smaller than the energy gain and energy barrier discussed above. Therefore, our LSDA total energy calculations show that the C_{Si}-V_C pair is energetically favored over the isolated silicon vacancy for all charge states except for the -4 charge state (Fig. 7).

The $+2$ and 0 charge states of the pair have a diamagnetic ground state and excited spin-triplet states. Hence, they are both candidates for the *P*6/*P*7 EPR signals resulting from an excited $S=1$ state.

In C_{3v} symmetry, the C_{Si}-V_C pair in its doubly positive charge state has a resonant $a_1(s)$ level about 0.8 eV below the valence band maximum (VBM) and a corresponding $a_1^*(s)$ antibonding resonant state in the conduction band at 4.5 eV above the VBM. Additionally, *p*-like $a_1(p)$ and $e(p)$ levels are induced in the band gap (Fig. 8). All a_1 levels arise mainly from the dangling bond of the carbon antisite. The *e* level stems from the dangling bonds of the silicon neighbors of the carbon vacancy (see also Fig. 8).

The ground state of the doubly positive charge state is a singlet $^1A_1$ where two electrons with antiparallel spin occupy the $a_1(s)$ level in the valence band. The *p*-like a_1 and *e* levels in the band gap are empty (Fig. 8). Photons with energies higher than about 1.15 eV (exp: 1.1 eV) can excite an electron from the $a_1(s)$ level in the valence band into the unoccupied $a_1(p)$ level in the band gap, inducing a strongly localized *s*-like hole in the valence band, thus forming an excited state $^1A_2$ (Fig. 8 and 9). A nonradiative transition to the energetically lower metastable triplet state $^3A_2$ is possible with the help of phonons (Fig. 9). This $^3A_2$ state gives

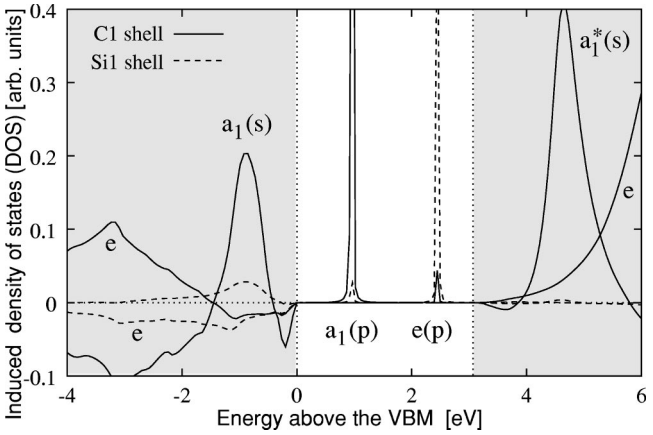

FIG. 8. Calculated induced density of states for the diamagnetic ground state of the C_{Si}-V_C pair in 6*H*-SiC (unrelaxed structure, charge state $2+$).

rise to the *P*6/*P*7 EPR spectra observed experimentally. The MCDA can be explained by the additional excitation of the $a_1(p)$ electron into the *e* state (Fig. 8). The calculated photon energy of the $^3A_2 \rightarrow {}^3E$ transition is 1.52 eV. (Note that excitation energies are not calculated from the one-particle energies discussed above, but from the differences in the LMTO total energies of the unrelaxed structures.) This exceeds the experimental values (1.0–1.1 eV), but an overestimation of the photon energies in this order is known for LMTO-ASA calculations in the framework of the LSDA.[23,24]

A similar excitation scheme is possible for the neutral charge state. In the $^1A_1$ ground state the $a_1(p)$ level is occupied with two electrons with antiparallel spin. If one of these electrons is optically excited into the *e* level, this results in an excited singlet state ^1E that can relax into the ^3E state with $S=1$. The ^3E state could also give rise to the photoexcited *P*6/*P*7 EPR spectra and could be the ground state of the MCDA transition. The optically allowed excitation of the second electron into the *e* level gives rise to the MCDA. As shown in Fig. 9, the calculated excitation energies are similar to the values already discussed for the excitation mechanism of the doubly positive charge state.

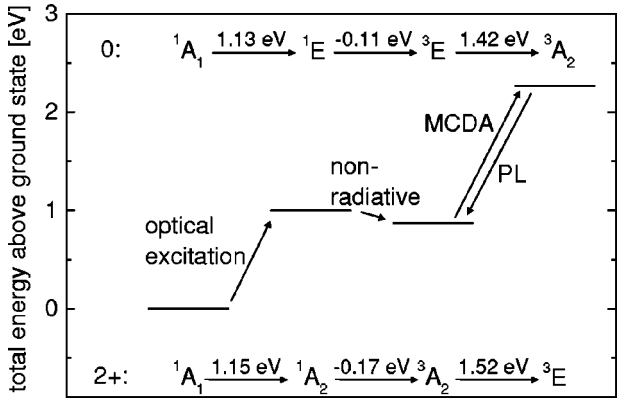

FIG. 9. Excitation schemes for the C_{Si}-V_C pair in the charge states 0 and $2+$. The transition energies are calculated from the differences of the total energies.

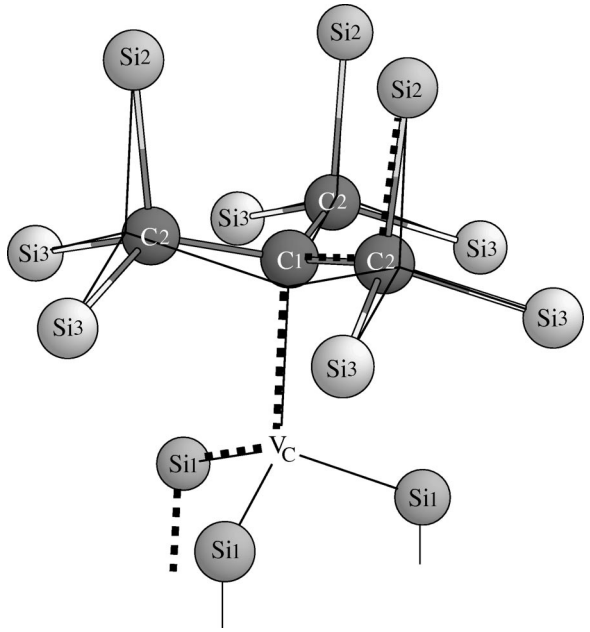

FIG. 10. Relaxed structure of $(C_{Si}\text{-}V_C)^{2+}$ in the $(^3A_2)$ excited state obtained from SCC-DFTB calculations. The thin lines mark the position of the bonds in the ideal lattice. The carbon antisite C1 relaxes by 16% of the bond length in the ideal crystal away from the vacancy. The dashed line marks the (1120) plane shown in Fig. 12.

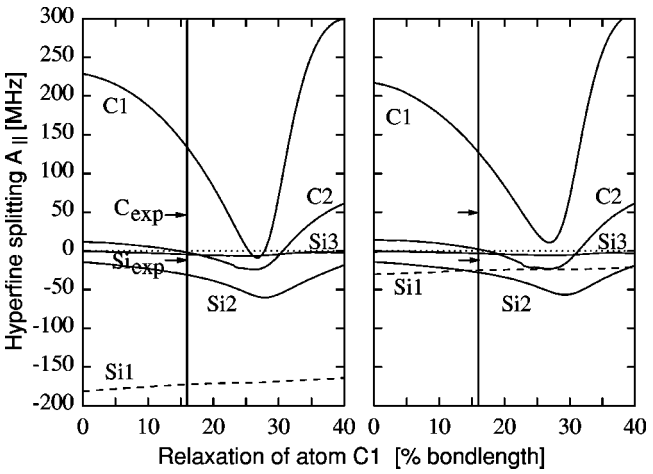

FIG. 11. Calculated hyperfine parameters $A_{||}$ for different nuclei around the defect as a function of the position of the carbon antisite. Left: neutral charge state, right: doubly positive charge state. The notation corresponds to Fig. 10. Vertical lines mark the minimal energy structure (16%). The small arrows indicate the experimental values. Note the difference in the hyperfine splitting of the Si1 nuclei (dashed line).

Therefore, both charge states of the defect can explain the excitation process observed experimentally. However, there remains one key to distinguish between these charge states—the comparison of the experimentally resolved hyperfine splittings with the theoretically calculated values.

To the hyperfine interactions there are contributions from the Fermi contact term, from the dipole-dipole interaction and from the orbital momentum. The latter is quenched to a high degree, which can be seen from a g value close to the free electron g value of 2.0023 and the long spin-lattice relaxation time T_1. Thus, it does not influence the hyperfine interactions in first order. This leaves us with the contributions from the Fermi contact term and the dipole-dipole interaction, both of which can be calculated directly from the magnetization density obtained from the LSDA spin density calculations.[26,36]

As mentioned above, lattice relaxations around a defect may strongly modify the magnetization densities and therefore the hyperfine interactions. For both charge states the relaxed defect geometries calculated with SCC-DFTB are quite similar. The silicon atoms relax inwards by 5%. The carbon antisite relaxes towards the plane of its carbon neighbors by 16% of the ideal bond length, resulting in an almost planar configuration (Fig. 10). This relaxation process is accompanied by a strong variation of the hyperfine interactions, especially with the carbon antisite nucleus. In Fig. 11 the hyperfine splittings depending on the position of the carbon antisite are calculated, leaving the other atoms on their relaxed positions as given by the SCC-DFTB calculations. The calculated value $A_{||}$ for the carbon antisite C1 approaches the experimental value of 48 MHz (represented by small horizontal arrows in Fig. 11) at a relaxation of 22% with respect to the ideal bond length, which is in qualitative agreement with the 16% relaxation predicted from SCC-DFTB calculations, especially having in mind that the energy minimum is rather shallow: the energy difference for these positions of C1 is less than 0.1 eV. In Fig. 11 the minimum energy structure is marked by a vertical line. For this geometry the hyperfine splittings due to the Si3 and C2 nuclei almost vanish for both charge states and would not be resolved from the central line (see also Fig. 6). Figure 12 shows that the magnetization density is mainly localized in p-like orbitals at the carbon antisite C1, leading to a rather large anisotropic hyperfine parameter b. Its value of about 25 MHz remains almost unaffected by the relaxation of the C1 nucleus. Thus, the variation in $A_{\|}=a+2b$ shown in Fig. 11 is mainly influenced by the change of the isotropic part a.

However, one significant difference in the hyperfine interaction constants emerges when considering the two possible charge states. For the neutral charge state, the calculated value of $A_{\|}\approx -180$ MHz for the silicon neighbors Si1 deviates strongly from the experimentally observed value of ± 12 MHz. This arises from an occupation of the e level, which is mainly localized at the Si1 atoms. Since no further satellite signals were measured in a region up to 2000 MHz, this charge state can be excluded.

In contrast, for the doubly positive charge state the e level remains unoccupied leading to a significantly lower magnetization density around the Si1 nuclei [see the white dot at the Si1 site in Fig. 12(b)]. The hyperfine interaction constants at the Si1 nuclei calculated for the $^3A_2$ state are reduced to 25 MHz, which is about the value of the Si2 atoms (Fig. 10)—in qualitative agreement with the experimentally observed values. The superposition of the hyperfine lines of Si1 and Si2 can explain the intensities of the inner hyperfine lines. A value of $15\pm 5\%$ agrees with an identification with six ^{29}Si nuclei (14.5%).

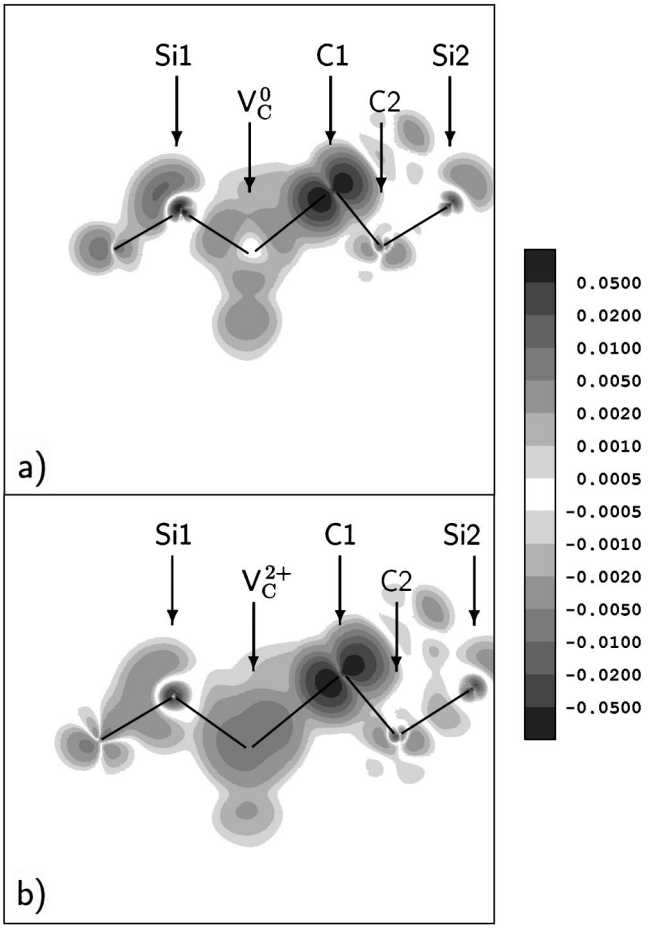

FIG. 12. Calculated induced magnetization density distribution of the relaxed (a) neutral and (b) the doubly positive C_{Si}-V_C structure in 6*H*-SiC in the (a) ^3E state and (b) the $^3A_2$ state.

VI. CONCLUSION

In this work we describe a nearest-neighbor pair defect in 6*H*-SiC (*P*6/*P*7 centers) which was observed on all inequivalent lattice sites and in all orientations. Its optical transitions were identified by MCDA-EPR. Experimentally, we have an intrinsic defect with a diamagnetic ground state, which has an excited triplet state about one eV above the ground state and a second excited triplet state, another one eV higher in energy. The lower triplet state shows a single prominent hyperfine interaction which is consistent with one ^{13}C nucleus, and a smaller hyperfine interaction that can be explained by four to eight ^{29}Si nuclei.

By means of theoretical calculations, we have checked several simple defect models that consist of aggregates of intrinsic defects. The C_{Si}-V_C defect in the doubly positive charge state explains the experimentally observed features (symmetry, hyperfine structure, optical properties, and defect formation) of the *P*6/*P*7 centers best. For the unrelaxed system, the calculated hyperfine interaction with the C_{Si} nucleus is more than four times larger than the value found experimentally, while with lattice relaxation we come much closer to the experimental values. The C_{Si}-V_C pair is therefore suggested as a suitable model for the *P*6/*P*7 centers.

In many respects the C_{Si}-V_C defect pair appears to be an ideal candidate for the annealing product of the V_{Si} defect, because it can be formed by the movement of a carbon ligand into the V_{Si}, it has a lower total energy than V_{Si} and a reaction barrier that matches the value found experimentally. There is, however, a problem left with the above identification that cannot be answered at the moment: we have not observed the *P*6/*P*7 defects prior to annealing. It is questionable that an irradiation process capable of producing isolated V_{Si} defects should not produce C_{Si}-V_C pairs. If the identification of the *P*6/*P*7 defects with C_{Si}-V_C pairs is correct, we must assume that these C_{Si}-V_C pairs are somehow removed during irradiation. We also cannot entirely exclude that the V_{Si} defect must be trapped at some other magnetically invisible defect structure, before *P*6/*P*7 defects can be formed or can be observed. We have, however, no hint for such a process.

In a next step, we shall try to establish that upon annealing the number of V_{Si} decreases by the same amount as the number of C_{Si}-V_C pair defects is raised. For this purpose we would need much finer annealing steps than used in the present study. These studies might also be helpful in answering the question of the invisibility of the *P*6/*P*7 defects directly after the irradiation.

Finally, we are left with the bad news that the C_{Si}-V_C defect, although diamagnetic in its ground state, is electrically and optically active. It has a charge transfer level just above midgap. Thus at least a second anneal step is required to remove the electrical activity of silicon-vacancy-related defects. The investigation of this second step, however, is beyond the scope of this paper.

ACKNOWLEDGMENTS

We thank Dr. E. N. Kalabukhova from the Institute of Semiconductor Physics, Kiev, Ukraine, for supplying the samples. This work was supported by the Deutsche Forschungsgemeinschaft.

[1] S. Onda, R. Kumar, and K. Hara, Phys. Status Solidi A **162**, 369 (1997).
[2] A. Edwards, D. N. Dwight, M. V. Ruo, M. C. Ridgway, G. Kelner, and N. Papanicolau, J. Appl. Phys. **82**, 4223 (1997).
[3] J. Schneider and K. Maier, Physica B **185**, 199 (1993).
[4] H. Itoh, M. Yoshikawa, I. Nashiyama, S. Misawa, H. Okumura, and S. Yoshida, IEEE Trans. Nucl. Sci. **37**, 1732 (1990).
[5] E. Sörman, N. T. Son, W. M. Chen, O. Kordina, C. Hallin, and E. Janzén, Phys. Rev. B **61**, 2613 (2000).
[6] M. Wagner, B. Magnusson, W. M. Chen, E. Janzén, E. Sörman, C. Hallin, and J. L. Lindström, Phys. Rev. B **62**, 16 555 (2000).
[7] T. Wimbauer, B. K. Meyer, A. Hofstaetter, A. Scharmann, and H. Overhof, Phys. Rev. B **56**, 7384 (1997).
[8] G. Cubiotti, Yu. Kucherenko, A. Yaresko, A. Perlov, and V. An-

tonov, J. Phys.: Condens. Matter **12**, 3369 (2000).
[9] E. Rauls, Th. Lingner, Z. Hajnal, S. Greulich-Weber, Th. Frauenheim, and J.-M. Spaeth, Phys. Status Solidi B **217/2**, R1 (2000).
[10] L. Torpo, R. M. Nieminen, K. E. Laasonen, and S. Pöykkö, Appl. Phys. Lett. **74**, 221 (1999).
[11] A. Zywietz, J. Furthmüller, and F. Bechstedt, Phys. Rev. B **62**, 6854 (2000).
[12] A. Zywietz, J. Furthmüller, and F. Bechstedt, Phys. Rev. B **59**, 15 166 (1999).
[13] V. S. Vainer and V. A. Il'in, Sov. Phys. Solid State **23**, 2126 (1981).
[14] N. T. Son, P. N. Hai, M. Wagner, W. M. Chen, A. Ellison, C. Hallin, B. Monemar, and E. Janzén, Semicond. Sci. Technol. **14**, 1141 (1999).
[15] N. T. Son, E. Sörman, W. M. Chen, C. Hallin, O. Kordina, B. Monemar, and E. Janzén, Phys. Rev. B **55**, 2863 (1997).
[16] Yu. A. Vodakov and E. N. Mokhov, U. S. Patent No. 4 147 572.
[17] O. Gunnarsson, O. Jepsen, and O. K. Andersen, Phys. Rev. B **27**, 7144 (1983).
[18] P. Deák, J. Miró, A. Gali, L. Udvardi, and H. Overhof, Appl. Phys. Lett. **75**, 2103 (1999).
[19] M. Lannoo and J. Bourgoin, *Point Defects in Semiconductors I (Theoretical Aspects)*, Springer Series of Solid State Sciences (Springer-Verlag, Heidelberg, 1981).
[20] G. A. Baraff and M. Schlüter, Phys. Rev. B **30**, 3460 (1984).
[21] F. Beeler, O. K. Andersen, and M. Scheffler, Phys. Rev. B **41**, 1603 (1990).
[22] U. von Barth, Phys. Rev. A **20**, 1693 (1979).
[23] U. Gerstmann, A. T. Blumenau, and H. Overhof, Phys. Rev. B **63**, 075204 (2001).
[24] U. Gerstmann, M. Amkreutz, and H. Overhof, Phys. Rev. B **60**, R8446 (1999).
[25] Th. Frauenheim, G. Seifert, M. Elstner, Z. Hajnal, G. Jungnickel, D. Porezag, S. Suhai, and R. Scholz, Phys. Status Solidi B **217**, 41 (2000).
[26] H. Overhof, M. Scheffler, and C. M. Weinert, Phys. Rev. B **43**, 12 494 (1991).
[27] J.-M. Spaeth, J. R. Niklas, R. H. Bartram, *Structural Analysis of Point Defects in Solids*, Springer Series of Solid State Sciences (Springer-Verlag, Heidelberg, 1992).
[28] N. M. Pavlov, M. I. Iglitsyn, M. G. Kosaganova, and V. N. Solomatin, Sov. Phys. Semicond. **9**, 845 (1975).
[29] A. Mattausch, M. Bockstedte, and O. Pankratov, Mater. Sci. Forum **353-356**, 323 (2001).
[30] L. Torpo and R. M. Nieminen, Mater. Sci. Eng., B **61-62**, 593 (1999).
[31] S. Pöykkö, M. J. Puska, M. Alatalo, and R. M. Nieminen, Phys. Rev. B **54**, 7909 (1996).
[32] M. Bockstedte and M. Scheffler, Z. Phys. Chem. (Munich) **200**, 195 (1997).
[33] K. H. Wietzke, F. K. Koschnick, and J.-M. Spaeth, Mater. Sci. Forum **196-201**, 1061 (1995).
[34] H. J. Sun, C. F. Rong, and G. D. Watkins, Phys. Rev. B **50**, 10 619 (1994).
[35] N. T. Son, P. N. Hai, and E. Janzén, Mater. Sci. Forum **353-356**, 499 (2000).
[36] U. Gerstmann, M. Amkreutz, and H. Overhof, Phys. Status Solidi B **217**, 665 (2000).